



CHALMERS
UNIVERSITY OF TECHNOLOGY

Self-healing properties of Ce/Co-coated stainless steel under simulated intermediate temperature solid oxide fuel cell conditions

Downloaded from: <https://research.chalmers.se>, 2024-03-13 09:10 UTC

Citation for the original published paper (version of record):

Goebel, C., Asokan, V., Khieu, S. et al (2021). Self-healing properties of Ce/Co-coated stainless steel under simulated intermediate temperature solid oxide fuel cell conditions. *Surface and Coatings Technology*, 428. <http://dx.doi.org/10.1016/j.surfcoat.2021.127894>

N.B. When citing this work, cite the original published paper.



Self-healing properties of Ce/Co-coated stainless steel under simulated intermediate temperature solid oxide fuel cell conditions

Claudia Goebel, Vijayshankar Asokan, Sarah Khieu, Jan-Erik Svensson, Jan Froitzheim^{*}

Chalmers University of Technology, Department of Chemistry and Chemical Engineering, Division of Energy and Materials, Kemivägen 10, SE-41296 Gothenburg, Sweden

ARTICLE INFO

Keywords:

Solid oxide fuel cell
Interconnect
Corrosion
Ce/Co coating
Cr-evaporation
Self-healing

ABSTRACT

The interconnects used in solid oxide fuel cells (SOFC) are usually shaped into a corrugated form that creates gas channels. Coatings are applied onto an interconnect to increase its longevity by reducing Cr(VI) evaporation and oxide scale growth. To date many manufacturers first deform the interconnect and then apply the coating. However, the reverse (hereinafter termed pre-coating) would be more cost-effective, because large-scale roll-to-roll coating processes could then be used instead of batch coating processes. The drawback of this method is that cracks are introduced into the coating during deformation. The present work shows that the cracks heal after relatively short exposure times for the often-used Ce/Co coating (10 nm Ce and 640 nm Co) even at low operating temperatures (650 °C and 750 °C). The Cr evaporation rate of pre-coated deformed Ce/Co-coated AISI 441, even though slightly elevated in the beginning of the exposure, decreases and stabilizes to rates that are comparable to that of undeformed Ce/Co-coated AISI 441. SEM micrographs show that the cracks introduced during the shaping of the interconnect heal after roughly 70 h of exposure at 750 °C and 360 h of exposure at 650 °C.

1. Introduction

Solid oxide fuel cell (SOFC) technology is a promising green energy conversion technique that could be highly relevant for the future [1,2]. However, it still suffers from major challenges, the biggest being cost. Besides refining the system as a whole to reduce cost, the improvement of certain components can also lead to further cost reduction. A major share of the overall cost of a fuel cell stack is the interconnect, which connects separate fuel cells to form a fuel cell stack and is typically made of ferritic stainless steel (FSS) [3–6]. This component has previously contributed to roughly 35% of the entire stack cost [7]. However, improvements; such as switching from tailor-made steels (e.g. Crofer 22 APU or ZMG232) to high volume products (e.g. AISI 441) or reducing the thickness of the interconnect; have reduced the interconnect cost drastically [8]. Further improvements are still needed both in terms of material cost and ease of manufacturing.

Nowadays the manufacturing of interconnects mostly remains a multiple-step batch process. First, the interconnect must be stamped into a manufacturer-specific design, and afterwards a coating is applied batchwise. Even though the coating composition varies from producer to producer, its function does not. Within the range of the most commonly used operating temperatures of SOFCs (600 °C - 850 °C), ferritic stainless

steels used as an interconnect material corrode heavily [6,9,10]. Coatings are applied onto the interconnect to avoid corrosion as well as related corrosion phenomena. Two main concerns are usually addressed with these coatings [11]. First, a coating should decrease oxide scale growth and ideally increase oxide scale adhesion, even during thermal cycling. Both of these factors can be addressed by applying a reactive element coating, such as Ce [12,13]. Reactive elements are often added as a minor alloying element to steel, but a more cost-effective method is to add a thin coating layer (≤ 50 nm) directly onto the steel. Second, the coating must mitigate Cr evaporation. Cr species that evaporate from the outer Cr_2O_3 layer of a FSS interconnect poison the cathode and lead to Cr depletion of the material [14]. Cathode poisoning occurs when gaseous Cr(VI) species block the triple phase boundaries in the cathode leading to fuel cell degradation [15,16]. Highly effective coatings that mitigate Cr-evaporation are spinel oxides, and the most commonly discussed and applied one is $(\text{Mn},\text{Co})_3\text{O}_4$ (MCO) [17–19]. Besides its great Cr retention properties, this coating is also highly conductive in comparison to other spinel oxides [20]; both of these are important characteristics of a good interconnect coating. Another advantage of this coating is that it can be applied as a conversion coating [21,22]. In contrast to a non-conversion coating for which the oxide is directly applied onto the steel using powder-based methods, conversion coatings rely on coating the steel

^{*} Corresponding author.

E-mail address: jan.froitzheim@chalmers.se (J. Froitzheim).

<https://doi.org/10.1016/j.surfcoat.2021.127894>

Received 25 August 2021; Received in revised form 3 November 2021; Accepted 4 November 2021

Available online 8 November 2021

0257-8972/© 2021 The Author(s). Published by Elsevier B.V. This is an open access article under the CC BY license (<http://creativecommons.org/licenses/by/4.0/>).

with a metal. This means that for the MCO coating, the Co is applied onto the interconnect, where it quickly oxidizes to form Co_3O_4 during high temperature exposure. Outward diffusion of Mn from the steel to the surface then leads to the formation of MCO. The great benefit of this coating route is that a large-scale roll-to-roll physical vapor deposition (PVD) process can be applied, in which large amounts of steel can be coated continuously [23,24]. This manufacturing route has the added advantage that very thin, and highly dense coatings can be obtained, and no extra densification step is required, as is often the case for non-conversion coatings [25,26]. However, if the interconnect is first stamped and then coated, the large-scale roll-to-roll process cannot be implemented. On the other hand, if the interconnect is first coated and then stamped (hereinafter called pre-coated), the coating will crack during deformation and this could lead to increased Cr evaporation or even delamination of the entire coating.

Falk-Windisch et al. [23,27] examined Ce/Co-coated material that had been pre-coated and found that the cracks, which had formed in the coating during deformation, had completely healed after only 24 h of exposure at 850 °C. According to those authors, this could be due to two processes that take place during exposure at high temperature. First, the oxidation of a Co coating led to an expansion of volume [28], which potentially healed cracks. Second, the Co interdiffused into larger cracks [23,27]. It was suggested that the latter process occurred as follows. The coated areas were initially covered with Co_3O_4 , which over time was enriched in Mn. In contrast the cracked areas were initially covered by a $(\text{Cr,Mn})_3\text{O}_4$ layer. The self-healing was accomplished by the fast lateral Co diffusion between these areas resulting in a homogenous $(\text{Co,Mn})_3\text{O}_4$ cap layer over the entire surface of the coated FSS. The Cr evaporation reported in [23,27] verified that the cracks healed extremely fast, and no significant difference in Cr evaporation was observed between the undeformed Ce/Co-coated FSS and the deformed Ce/Co-coated FSS. However, even though the process of self-healing occurs rapidly at 850 °C and therefore large-scale roll-to-roll manufacturing processes could be used at these operating temperatures, it remained very doubtful if the healing process also occurred at lower operating temperatures. This was mainly due to the fact that the self-healing mechanism relies heavily on lateral Co diffusion along the surface of the coated material. Data by Grzesik et al. [29] suggests that the diffusion of Co ions is one to two orders of magnitude lower at 650 °C than at 850 °C. Therefore, the self-healing mechanism might be too slow at 650 °C to effectively inhibit Cr poisoning. This question is especially important, because lower operating temperatures are highly relevant from a technical perspective as they might allow for the use of cheaper materials, for example, the tailor-made and, thus, expensive Crofer 22 APU can be substituted with the much cheaper and commercially available FSS AISI 441 [30].

The present work builds on the work by Falk-Windisch et al. [23,27] and investigates if SOFCs operating at intermediate temperatures (IT-SOFC), i.e. 650 to 750 °C, also allow for the use of pre-coated FSS and if self-healing occurs at these low temperatures. Ce/Co-coated AISI 441 was used (10 nm Ce/640 nm Co) for this purpose, and Cr evaporation and the microstructural properties of biaxially deformed material were compared to those of undeformed material at two different exposure temperatures, 650 °C and 750 °C. Biaxial deformation was chosen, because the cracks formed by this deformation technique are similar to cracks formed during the stamping of an interconnect in terms of directionality and size [27].

2. Materials and methods

2.1. Sample preparation

The ferritic stainless steel AISI 441 was used for all exposures conducted within the scope of this work. Three different sets of samples were investigated: uncoated and undeformed AISI 441, Ce/Co-coated undeformed AISI 441, and Ce/Co-coated biaxially deformed AISI 441. The chemical composition of AISI 441 is shown in Table 1. AISI 441 was available as 0.2 mm thick sheets. The Ce/Co coating was applied by Sandvik Materials Technology (SMT) using a proprietary PVD technique. First 10 nm of metallic Ce was applied and afterwards 640 nm of metallic Co was applied. For the deformed samples, AISI 441 was first coated by SMT and then biaxially deformed using the Erichsen test of deep drawing, which is schematically shown in [31]. The deformation resulted in a decrease in sample thickness, with the new material thickness being 0.17 mm. The area that lacks a coating due to deformation was estimated to be 20% using image analysis of Co maps obtained by EDX on unexposed material. Square samples, 1.5 cm by 1.5 cm, were cut from the steel sheets, which resulted in uncoated edges, and these samples were cleaned ultrasonically in acetone and ethanol. Afterwards, Cr evaporation was measured according to the specifications below. Some samples were heat-treated prior to measuring the Cr evaporation. This heat-treatment was implemented because in a real fuel cell the stack would be sealed at temperatures around 800 °C \pm 75 °C (manufacturer-dependent). Therefore, introducing a heat treatment prior to exposure simulates the real fuel cell conditions. Heat treatment was carried out at 850 °C for 3 h in humid air (3% H_2O) with a high flow rate of 6000 $\text{sml} \cdot \text{min}^{-1}$.

2.2. Cr evaporation

In-situ Cr evaporation was measured according to a denuder technique first reported by Froitzheim et al. [32]. Using this technique, the evaporated Cr species was quantified by the reaction of hexavalent Cr with Na_2CO_3 . The mass of the subsequently formed Na_2CrO_4 was then determined by measuring the concentration of a Na_2CrO_4 -containing solution using UV-Vis Spectrophotometry (Thermo Scientific Evolution™ 60S).

For each exposure, three samples were placed in a tubular furnace with a high flow (6000 $\text{sml} \cdot \text{min}^{-1}$) of air containing 3% water vapor. Three different temperatures were investigated in the present work, 850 °C, 750 °C, and 650 °C. Cr evaporation was measured at all temperatures for uncoated AISI 441, Ce/Co-coated undeformed AISI 441, and Ce/Co-coated biaxially deformed AISI 441. Additionally, Ce/Co coated biaxially deformed AISI 441 that was heat-treated prior to conducting Cr-evaporation measurements, was investigated at 650 °C. Experiments were carried out for 500 h. Additional short exposures were conducted for 71 h at 750 °C and 111 h at 650 °C to document the progress of the self-healing properties of the Co coating further. The time lengths for these short exposures were chosen because they coincide with the first denuder change.

No further analysis was performed for exposures at 850 °C, and the reader is referred to previous work reported by Falk-Windisch et al. [23,27]. For all other specimens, further characterization was carried out as follows.

2.3. Electron microscopy

Selected samples were investigated with electron microscopy before

Table 1

Composition of AISI 441 used in the present work in weight%. For uncoated AISI 441 a different batch was used.

AISI 441/EN 1.4509	Fe	Cr	Mn	Si	Ti	Nb	C	S	P	N
	Bal.	17.61	0.28	0.59	0.153	0.39	0.017	0.001	0.029	0.012

and after Cr evaporation measurements. Different microscopes and milling techniques were used for this purpose. All top-view micrographs and the corresponding elemental maps were recorded using a FEI Quanta 200 FEG environmental scanning electron microscope (SEM) equipped with an Oxford Instruments X-Max^N energy dispersive x-ray spectroscopy (EDX) detector. This microscope was also used for cross-sections that were prepared with broad ion beam (BIB) milling using the Leica EM TIC 3X. For biaxially deformed samples exposed for intermediate times, i.e. 71 h at 750 °C and 111 h at 650 °C, in-situ lift-outs were prepared using the FEI Versa 3D DualBeam focused ion beam/scanning electron microscope (FIB/SEM). Pt deposited on the areas of interest protected the sample surface from damage caused by the ion beam milling process. The lift-outs were further analyzed with scanning transmission electron microscopy (STEM) utilizing a FEI Titan 80–300 transmission electron microscope (TEM) equipped with an INCA X-sight Oxford Instruments EDX detector. High-Angle Annular Dark-Field imaging (HAADF) was utilized.

3. Results

3.1. Cr evaporation

The Cr evaporation rates of all investigated samples are depicted as a function of exposure time in Fig. 1. To understand the development of the Cr evaporation rate over time, the bottom row (Fig. 1a1, b1, c1) shows the same results as the top row, but with a magnified y-axis. All exposures were carried out for 500 h, except for the Cr evaporation rates depicted as filled symbols, which were run for the intermediate times, i.e. 71 h at 750 °C and 111 h at 650 °C. The reason different time intervals had to be employed for the two different temperatures was the rather

small amounts of hexavalent Cr species that evaporated at 650 °C in combination with the sensitivity of the UV–Vis analysis.

Figure 1a and a1 show the results for AISI 441 exposed to air at 850 °C. The Cr evaporation rate for the uncoated material decreased slightly in the beginning, but after roughly 90 h of exposure, no further change in rate was visible, and an average rate of $3.5 \cdot 10^{-4} \text{ mg cm}^{-2} \text{ h}^{-1}$ was found. The Cr evaporation rates for Ce/Co-coated AISI 441 decreased by roughly a factor of 10 compared to the uncoated AISI 441, and the average rate was around $3.2 \cdot 10^{-5} \text{ mg cm}^{-2} \text{ h}^{-1}$. Undeformed and deformed Ce/Co-coated AISI 441 showed a significant scatter in Cr evaporation rate at 850 °C, but no clear trend could be detected between the deformed versus undeformed material.

The Cr evaporation rate at 750 °C is shown in Fig. 1b and b1. The rate for uncoated AISI 441 at this temperature was on average $1.4 \cdot 10^{-4} \text{ mg cm}^{-2} \text{ h}^{-1}$. The first data point is not included in this average value because a decrease in rate was visible in the beginning. A slight difference in the Cr evaporation rate behavior was visible between the undeformed and deformed Ce/Co-coated AISI 441 that was exposed to air at 750 °C. The Cr evaporation rate was nearly constant with an average rate of $1.2 \cdot 10^{-5} \text{ mg cm}^{-2} \text{ h}^{-1}$ for the undeformed material. On the other hand, the initial average Cr evaporation rate for the deformed Ce/Co-coated AISI 441 was $2.1 \cdot 10^{-5} \text{ mg cm}^{-2} \text{ h}^{-1}$, however, this rate quickly decreased by a factor of 1.75, and both the deformed and undeformed Ce/Co-coated AISI 441 showed similar Cr evaporation rates after only 168 h.

Fig. 1c and c1 depict the Cr evaporation rate for AISI 441 exposed to air at 650 °C. The Cr evaporation rate for the uncoated material decreased in the beginning, and a plateau seemed to be reached after more than 360 h of exposure. The rate after the decrease was around $7.8 \cdot 10^{-5} \text{ mg cm}^{-2} \text{ h}^{-1}$. Ce/Co-coated AISI 441 exhibited much lower Cr

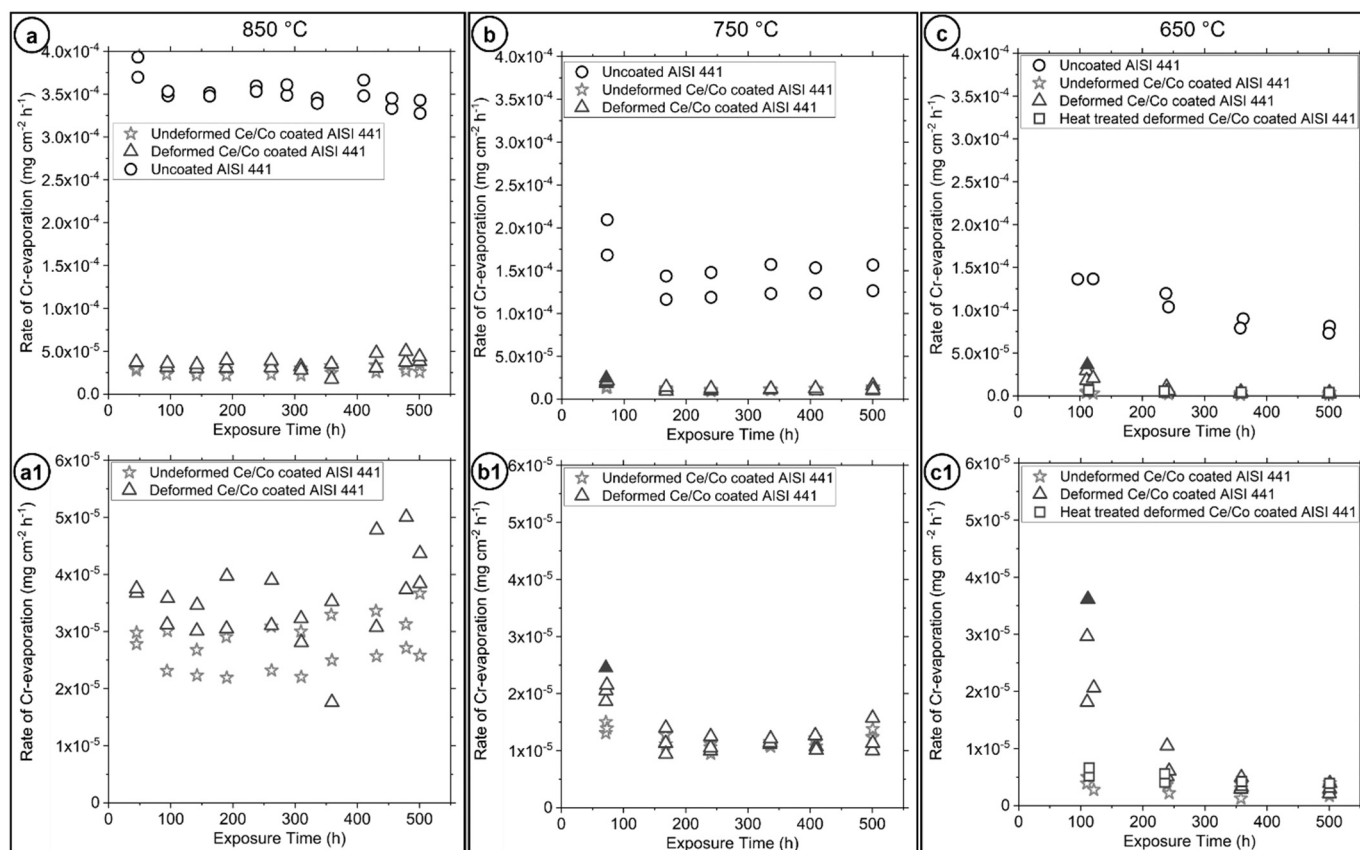


Fig. 1. Cr evaporation rates for uncoated and Ce/Co-coated AISI 441. Samples were exposed to air at 850 °C (a and a1), 750 °C (b and b1), and 650 °C (c and c1). The bottom row depicts zoomed in versions of the top row. Filled symbols mark samples that were taken out after 71 h or 111 h of exposure at 750 °C or 650 °C, respectively.

evaporation rates than the uncoated material. However, the initial rates for the deformed Ce/Co-coated AISI 441 were substantially higher ($2.6 \cdot 10^{-5} \text{ mg cm}^{-2} \text{ h}^{-1}$) than those for the undeformed Ce/Co-coated AISI 441 ($3.3 \cdot 10^{-6} \text{ mg cm}^{-2} \text{ h}^{-1}$). Nevertheless, after 360 h of exposure, the rates for the deformed material had decreased by a factor of 6–8 and had reached the same level as those for the undeformed material. At 650 °C Cr-evaporation measurements were also conducted on heat-treated deformed Ce/Co coated AISI 441. The rates for these samples were similar to those of undeformed Ce/Co coated AISI 441 throughout the exposure, even in the initial phases.

As mentioned in the experimental part (see Section 2.1) uncoated edges were present for all coated samples due to experimental limitations. These uncoated edges might increase the Cr-evaporation slightly. Nevertheless, this does not influence the outcome of the present study, because both deformed and undeformed Ce/Co coated AISI 441 had uncoated edges resulting in a similar evaporation from the edges for both types of samples.

3.2. Micro-structural investigation

SEM micrographs of unexposed Ce/Co-coated AISI 441 are depicted in Fig. 2. For the undeformed material, Fig. 2a, the surface was homogenous and no cracks in the coating were found. However, the rolling direction of the underlying steel was visible. In contrast cracks were clearly visible on the entire surface of the deformed material, shown in Fig. 2b. The FIB-milled cross-section of the biaxially deformed Ce/Co coated AISI 441 confirmed that cracks (indicated by arrows in Fig. 2c) had formed in the coating.

The SEM micrographs of 500 h exposed undeformed Ce/Co-coated

AISI 441 are shown in Fig. 3. They confirm that even after 500 h of exposure, the homogeneity and uniformity of the surface morphology for undeformed Ce/Co-coated AISI 441 was similar regardless if the material was exposed at 750 °C (Fig. 3a) or at 650 °C (Fig. 3b). Additionally, the rolling direction of the underlying steel was no longer visible after 500 h of exposure.

SEM micrographs of the deformed Ce/Co-coated AISI 441 that was exposed at 750 °C are shown in Fig. 4. The cracks that had formed during the biaxial deformation of Ce/Co-coated AISI 441 are still very clearly visible on the surface of the samples in the figure, even after 500 h of exposure (see Fig. 4a). However, the corresponding EDX maps showed that the entire surface was already covered with Co, and no Fe or Cr signal was recorded from the underlying steel. This indicates that a thick Co oxide had formed also inside the cracks of the coating. Locally higher Mn concentrations were also recorded. The BIB-milled cross-section of this sample (see Fig. 4b) showed that in some areas the Cr-rich scale was not yet covered by a thick $(\text{Co, Fe, Mn})_3\text{O}_4$ scale after 500 h (see orange circle in inset in Fig. 4b).

To further understand how quickly Co had diffused into the cracks of deformed Ce/Co-coated AISI 441 at 750 °C, short-term exposed samples, 71 h, were analyzed further. In situ lift-out samples were prepared for this purpose using FIB and were examined using STEM/EDX, and the results are depicted in Fig. 5. The EDX map and line scan for the cracked region are shown in Fig. 5c. Additional line scans performed in multiple places throughout the lift-out in cracked and non-cracked regions were used to determine the cationic% stated below and in Table 2. The line scans were performed using higher magnification than what is depicted in Fig. 5.

A Co,Mn oxide had formed in non-cracked regions with a thickness of

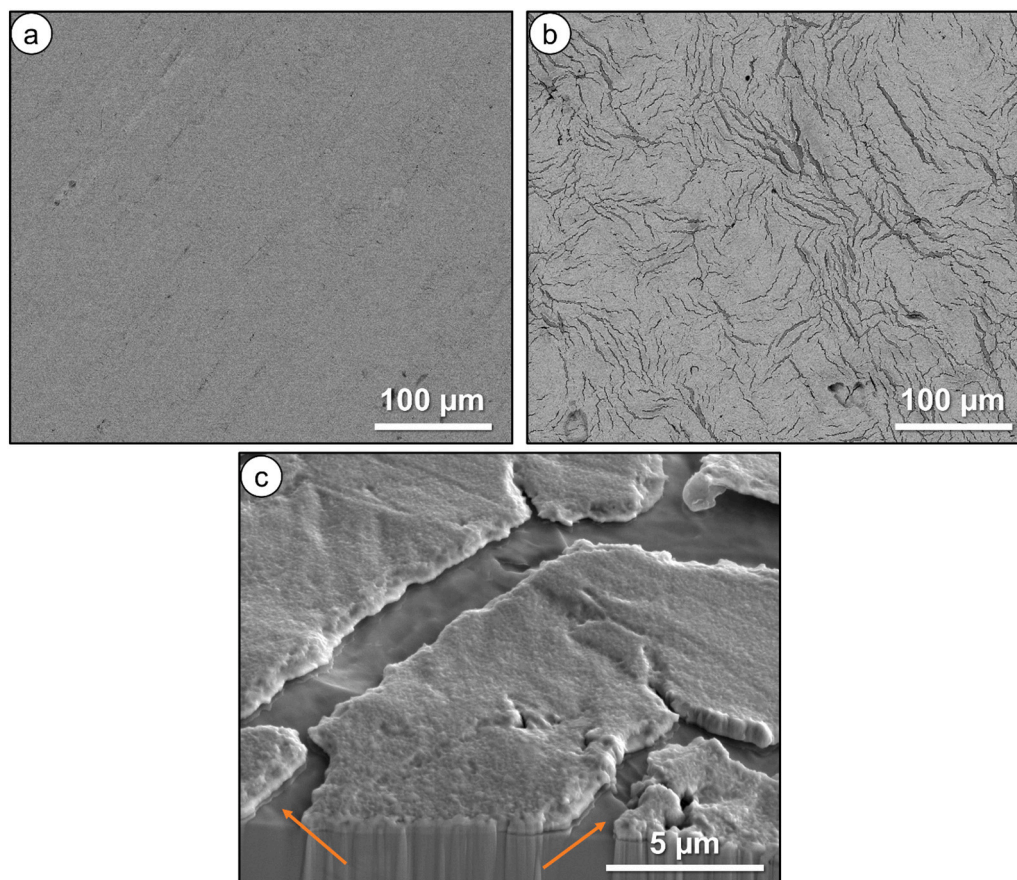


Fig. 2. Backscattered SEM micrograph for unexposed Ce/Co-coated AISI 441. The samples were either undeformed (a), or biaxially deformed (b and c). A) and b) correspond to top-view micrographs of the respective samples, and b) corresponds to a FIB-milled cross-section of a biaxially deformed sample. The arrows in c) indicate the location of cracks in the coating.

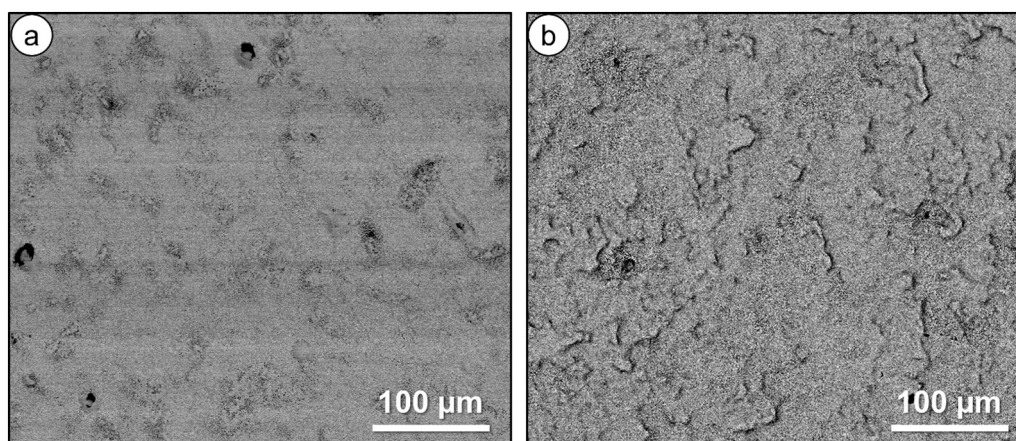


Fig. 3. Backscattered SEM micrograph of undeformed Ce/Co-coated AISI 441 that was exposed to air for 500 h either at 750 °C a) or at 650 °C b).

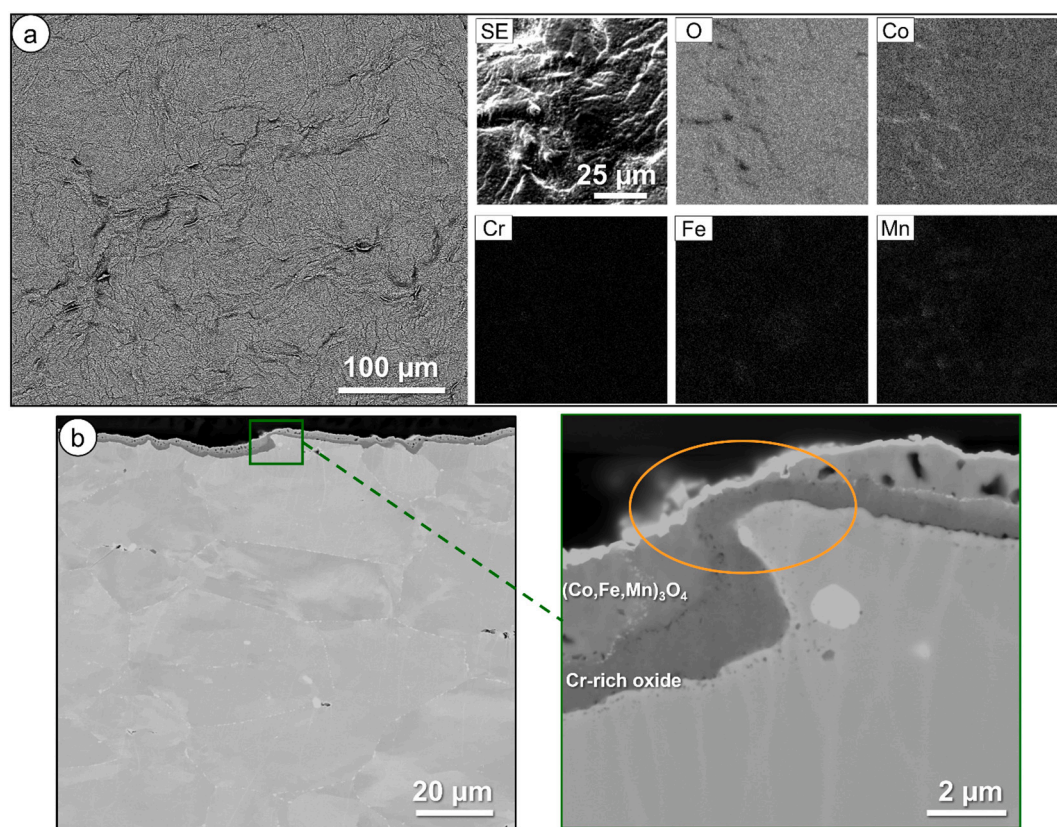


Fig. 4. SEM micrographs and quantitative EDX maps (at.%) of biaxially deformed Ce/Co-coated AISI 441 that was exposed to air for 500 h at 750 °C. A) corresponds to a top-view of the sample, and b) corresponds to a BIB-milled cross-section of the same sample. The circle in the inset (b) shows the area where the crack in the coating was located and $(\text{Co,Fe,Mn})_3\text{O}_4$ had not yet formed (in sufficient thickness) on top of the Cr-rich scale.

approximately 1.2 µm, and roughly 92 cationic% Co, 5 cationic% Mn, and low incorporations of Fe (below 3 cationic%). A thin Ce oxide layer was present below this oxide. The innermost layer consisted of a relatively pure Cr oxide scale (~280 nm) with low amounts of Mn, ranging between 1 and 4 cationic%.

Cracked regions (see Fig. 5) were also completely covered with a Co-rich oxide (marked as region I in the graph in Fig. 5c), with a thickness ranging between 300 and 400 nm and with 40–60 cationic% Co, 20–30 cationic% Mn, around 7 cationic% Fe, and, towards the inner oxide, increasing levels of Cr, from 0 cationic% at the outermost layer to 40 cationic% at the innermost layer of the Co,Mn-oxide. A pure and continuous, roughly 230 nm thick, Cr oxide (marked as region II in the

graph in Fig. 5c) had formed beneath this Co-rich oxide. Ce was only found in low quantities below 1 cationic% in the cracked region and did not show up at all in the EDX maps for this region.

The Fe, Cr, and O signals detected above the pure and dense Pt deposit are believed to be the redeposition that occurred during the milling process and can thus be ignored.

Fig. 6a shows top-view SEM micrographs of deformed Ce/Co-coated AISI 441 that was exposed for 500 h at 650 °C. The cracks were still clearly visible after 500 h of exposure at 650 °C, similar to the samples exposed at 750 °C (see Fig. 4a). However, contrary to the EDX maps recorded for the latter temperature, the EDX maps for samples exposed at 650 °C also still clearly showed the presence of cracks. Nevertheless, a

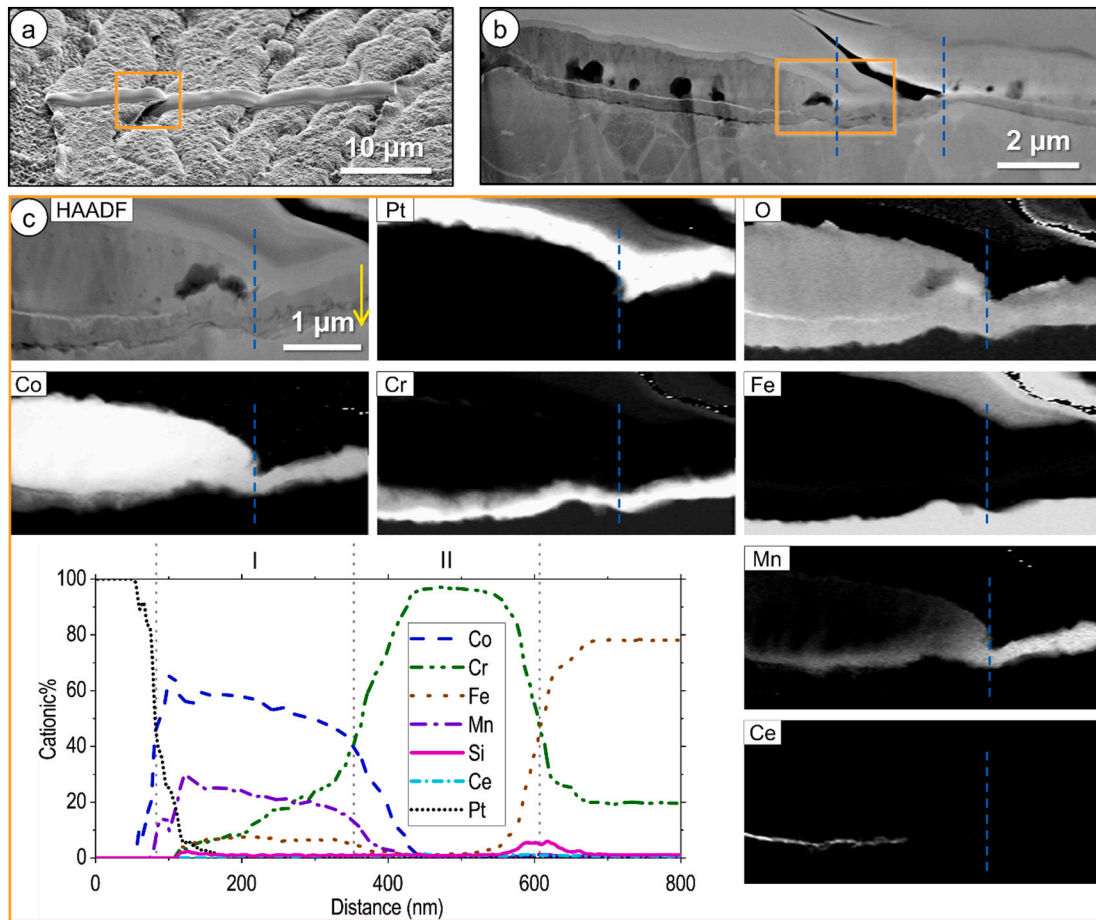


Fig. 5. Electron microscopy of biaxially deformed Ce/Co-coated AISI 441 that was exposed to air for 71 h at 750 °C. The crack marked by the orange box was investigated with STEM/EDX. A) SEM micrograph with Pt deposited on the area chosen for the FIB lift-out; b) HAADF micrograph of lift-out, with the area inside of the blue dashed lines marking the cracked area; c) HAADF micrograph including the corresponding EDX maps in at.% and a line scan through the crack (yellow arrow). The Si map is not shown in the EDX maps, as it was not relevant to the discussion. The cracked area is on the right side of the blue dashed line, while the non-cracked area is on the left side of it. (For interpretation of the references to color in this figure legend, the reader is referred to the web version of this article.)

Table 2

Composition of the oxides of deformed Ce/Co coated AISI 441 in cationic% based on Figs. 5c and 8c.

	71 h at 750 °C				111 h at 650 °C			
	Non-cracked region		Cracked region		Non-cracked region		Cracked region	
	Co-rich (~1.2 µm)	Cr-rich (~280 nm)	Co-rich (300–400 nm)	Cr-rich (230 nm)	Co-rich (~1.2 µm)	Cr-rich (~60 nm)	Co-rich (~30 nm)	Cr-rich (~20 nm) ^b
Co	92		40–60		Bal		≤30	20 → 0 ^a
Cr		Bal	0 → 40 ^a	~100		~100	5 → 30	≤70
Fe	≤3		~7				35–40	≥18
Mn	5	1–4	20–30		0 → 2 ^a		~15	11 → 5 ^a

^a The arrow indicates that the cationic% changes from the outer (left value) to the inner layer (right value) of the oxide.

^b Due to the thinness of this Cr-rich oxide scale the compositional values were probably influenced by the surroundings of the oxide, namely the Co-rich oxide and the steel. This makes these values unreliable.

small concentration of Co had already diffused into the cracks also at 650 °C, according to the Co map shown in Fig. 6. For deformed samples exposed at 650 °C nodules on the sample surface had formed and are indicated by arrows in Fig. 6. Further analysis of these nodules can be found below. Additionally, also heat-treated deformed Ce/Co coated AISI 441 that was exposed for 500 h at 650 °C was analyzed using SEM. The corresponding micrographs are depicted in Fig. 6b. Similar to the non-heat-treated samples, the cracks were still clearly visible after 500 h of exposure for heat-treated samples. However, no nodule formation had occurred in the latter samples.

SEM micrographs and EDX maps and line scans of the BIB cross-

section of biaxially deformed Ce/Co-coated AISI 441, which was exposed at 650 °C, are depicted in Fig. 7. The overview of the entire cross-section (Fig. 7a) shows that besides cracks (marked as i), also nodules (marked as ii) are clearly visible. Magnified micrographs show both areas in more detail (see Fig. 7b and c). The EDX maps of the BIB cross-section of the nodule is shown in Fig. 7c. The figure shows that four different regions were present inside the oxide nodule. An EDX line scan also confirmed this and the compositions of the different regions are given in Table 3. The first region in the EDX line scan (marked as I) showed high Au content, which was used to mark the surface of the cross-section. Region II is the actual surface of the nodule. The EDX line

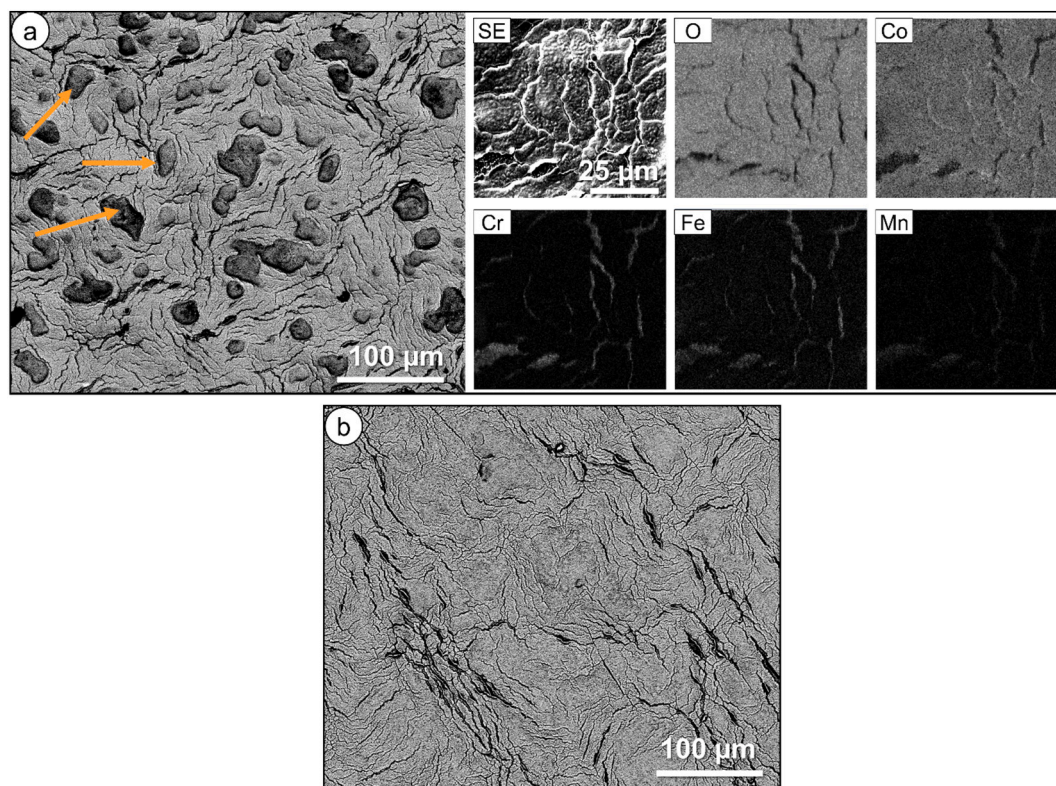


Fig. 6. SEM micrographs and quantitative EDX maps (at.%) of biaxially deformed Ce/Co-coated AISI 441 that was exposed to air for 500 h at 650 °C. A) was not heat-treated prior to exposure, whereas b) was heat-treated for 3 h at 850 °C prior to exposure.

scan showed that a thin (0.4 µm) Co-rich top layer had formed in this region with roughly 10 at.% incorporation of Fe. First a Fe,Co-rich oxide (marked as III) and then a rather pure Fe oxide (marked as IV) were present below this layer. According to the recorded EDX maps and the corresponding SEM micrograph, the thickness of the former oxide (Layer III) was roughly around 1.5 µm throughout the entire nodule, whereas the thickness of the latter layer (Layer IV) varied throughout the nodule. The bottom oxide scale of the nodule, which consisted of a Cr-rich oxide (marked as V), also showed this variation in thickness, and is assumed to be $(\text{Cr,Fe,Mn})_2\text{O}_3$ with roughly 10 to 20 at.% of Fe incorporation along with low levels of Mn (up to 3 at.%). The region VI marks the steel substrate. The inset inside the EDX line scan graph (see Fig. 7c) also shows that a thin Ce layer was detected in the cross-section; this layer can also be seen in the corresponding SEM micrograph and is marked as α (see Fig. 7c).

Short-term exposed specimens, 111 h, were also prepared for the deformed Ce/Co-coated AISI 441 that was exposed at 650 °C, and a FIB lift-out was analyzed using STEM/EDX. The results are shown in Fig. 8, and again multiple line scans were performed and form the basis for the cationic% stated below and in Table 2. The line scans were performed using higher magnification than what is depicted in Fig. 8.

The non-cracked region showed a pure Co oxide as the top layer, with a thickness of around 1.2 µm and only minor incorporation of Mn (around 2 cationic%) close to the innermost layer of this oxide. A Ce oxide scale had formed underneath this scale, beneath which a pure roughly 60 nm thick Cr oxide was present.

The Co signal for the cracked region suggests that small amounts of Co had diffused into the crack. A very thin Co oxide layer (marked as region I in the graph in Fig. 8c) had formed (~30 nm) on top of the crack, and up to 30 cationic% Co was found in this layer. Similar to the specimen that was exposed for 71 h at 750 °C, higher amounts of Mn, around 15 cationic%, seemed to be present in the Co-rich oxide covering the cracked area compared to the one covering the non-cracked area.

Additionally, high amounts of Fe, between 35 and 40 cationic%, were found in the Co-rich oxide, and increasing amounts of Cr were found in this oxide, from 5 cationic% in the outermost layer to 30 cationic% in the innermost layer. A Cr-rich oxide (marked as region II in the graph in Fig. 8c) had formed underneath the Co-rich oxide. However, unlike at 750 °C, this Cr-oxide was not pure and comparatively high amounts of Mn, Co, and Fe were present. Due to the thickness of this oxide (around 20 nm), it cannot be excluded that the EDX signal was influenced by the surroundings, i.e. the Co-rich oxide, the substrate, or the area underneath the surface. Again, no Ce signal was detected directly in the crack in the EDX maps, however low amounts were detected using the line scan (below 2 cationic%).

4. Discussion

The present study showed that when Ce/Co-coated ferritic stainless steels were deformed, cracks appeared in the coating (see Fig. 2). However, Cr evaporation data showed that these cracks quickly healed at 850 °C, because the Cr evaporation rate for the deformed material did not greatly differ from the rate for the undeformed material within the limits of the measurement technique (see Fig. 1a and a1). This self-healing process is consistent with previously reported data by Falk-Windisch et al. [23,27]. Their studies have shown that a Co-rich oxide forms on the entire surface of deformed Ce/Co-coated FSS at 850 °C after only 24 h of exposure. Additionally, their Cr evaporation data showed no difference between the pre-coated deformed Ce/Co-coated FSS and the undeformed Ce/Co-coated FSS, similar to the present study. Their assumption was that cracked regions first form a $(\text{Cr,Mn})_3\text{O}_4$ top layer and a subsequent interdiffusion of Co between this spinel in the cracked areas and the thick Co_3O_4 spinel in the non-cracked areas leads to the formation of a $(\text{Co,Cr,Mn})_3\text{O}_4$ spinel in the cracked areas with low levels of Cr. In Falk-Windisch et al.'s [23,27] studies the outer layer was uniformly covered by a pure $(\text{Co,Mn})_3\text{O}_4$ layer after 336 h of exposure, and

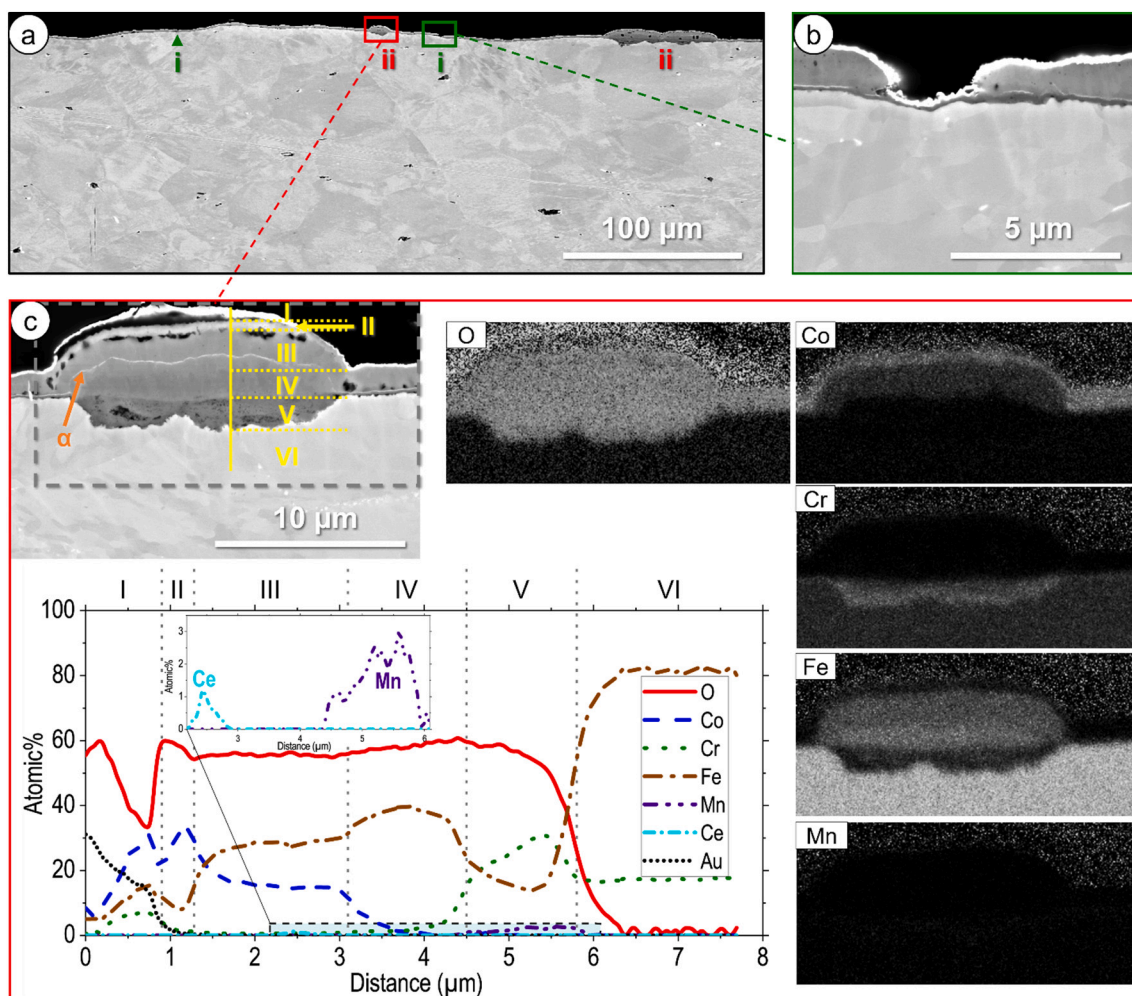


Fig. 7. Backscattered SEM micrographs and quantitative EDX maps (at.%) of BIB milled cross-sections of biaxially deformed Ce/Co-coated AISI 441, which was exposed to air for 500 h at 650 °C. Magnified micrographs for the cracked sections and the nodules found in the overview a) are shown in b) (marked as i) and c) (marked as ii), respectively.

Table 3

Composition of the regions found in the nodules that had formed on deformed Ce/Co coated AISI 441, which was exposed for 500 h at 650 °C in at.% based on Fig. 7c. Region I was excluded as this region still showed copious amounts of Au, which was used to mark the surface.

	Region II (0.4 μm)	Region III (1.5 μm)	Region IV (varying thickness)	Region V (varying thickness)	Region VI (steel substrate)
Ce	—	≤1	—	—	—
Co	20 → 33 ^a	21 → 15 ^a	10 → 0	—	—
Cr	—	—	—	20 → 32 ^a	~18
Fe	~10	~29	~38	10–20	82
Mn	—	—	—	≤3	—
O	60 → 55 ^a	56	56	56	—

^a The arrow indicates that the cationic% changes from the outer (left value) to the inner layer (right value) of the oxide.

the self-healing process was completed. The Cr evaporation rate found at 850 °C in the present work for uncoated AISI 441, the undeformed Ce/Co-coated AISI 441, and the biaxially deformed Ce/Co-coated AISI 441 matched well with data reported on Crofer 22 APU [23]. The reduction in the Cr evaporation rate by a factor of 10 between uncoated and coated AISI 441 has otherwise been well established [14,22,32,33]. For further

in-depth discussion of the self-healing process at 850 °C, including a microstructural analysis, the reader is referred to [23,27].

In the present work, non-cracked regions of samples that were exposed at 750 °C and 650 °C had formed a thick Co,Mn oxide scale on top of a thermally grown Cr oxide scale, which was concluded to be (Co, Mn)₃O₄ based on previous studies [33–35] with similar coatings. The thickness of the Co oxide scale (1.2 μm) was in accordance with the Pilling-Bedworth ratio of 1.98 for Co₃O₄ [36]. The extremely low incorporations of Mn in the Co oxide scale are similar to values reported by Falk-Windisch et al. [37] for both temperatures. The Cr oxide thickness found in the present work is also comparable to their findings [37]. A more in-depth analysis of the Ce/Co-coated undeformed material, which was exposed at 650 °C and 750 °C can be found in [37]. Falk-Windisch et al. used Sanergy HT instead of AISI 441, but these coated materials can be expected to exhibit similar oxidation behavior, as both materials contain similar levels of the most relevant alloying elements, especially Mn, and the coating used in the present work was the same as in [37].

While the formation of a thin Cr rich surface oxide in the of cracked areas occurred in a matter of hours at 850 °C (see Fig. 1a and a1), the process was much slower at lower temperatures and can, thus, be clearly seen in the development of Cr evaporation rates over time (see Fig. 1b, b1, c, and c1). This matches well to data by Grzesik et al. [29], which suggest that the diffusion coefficient drops by 1–2 orders of magnitude when the temperature is lowered from 850 °C to 650 °C. Nevertheless, even though the self-healing process was slower at 750 °C and 650 °C

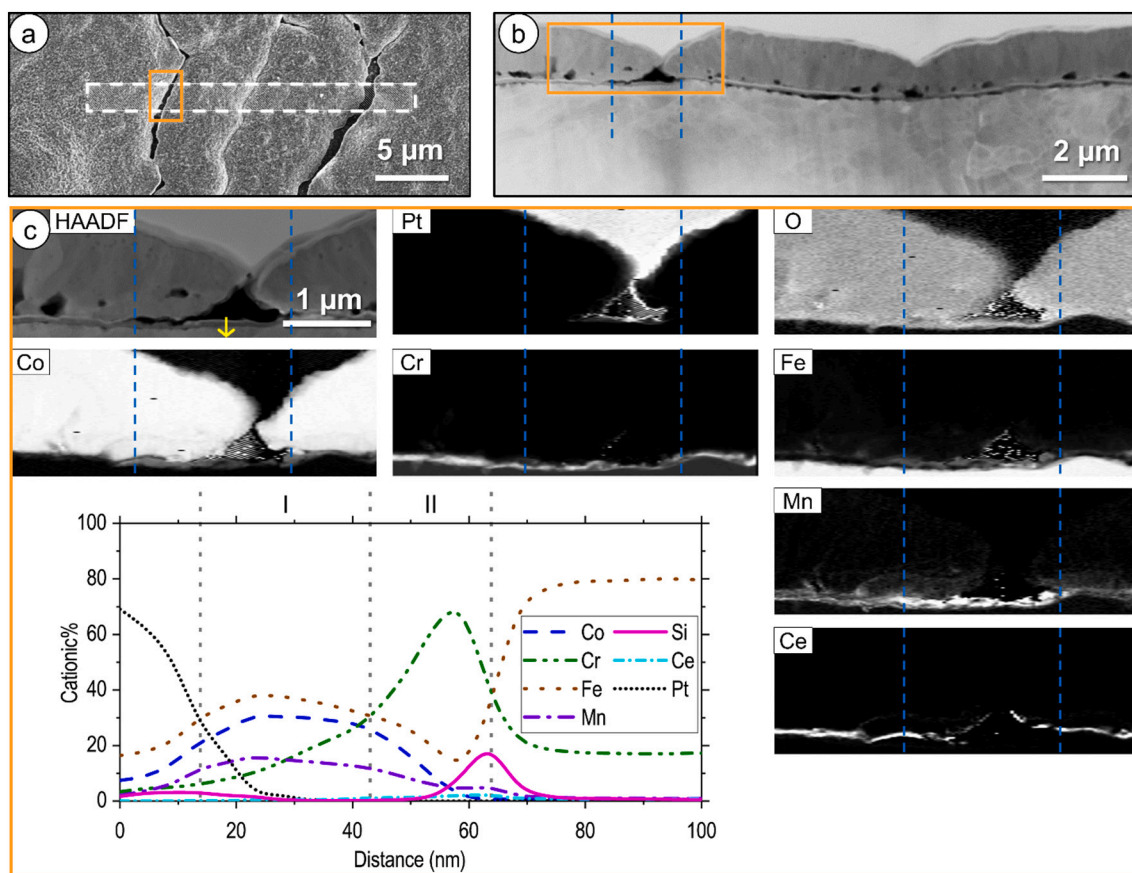


Fig. 8. Electron microscopy of the biaxially deformed Ce/Co-coated AISI 441 that was exposed to air for 111 h at 650 °C. The area marked by the orange box was investigated with STEM/EDX and the blue lines mark the crack location. A) SEM micrograph with the area chosen for the FIB lift-out marked by the dashed white box; b) HAADF micrograph of lift-out; c) HAADF micrograph including the corresponding EDX maps in at.% and a line scan through the crack (yellow arrow). The Si map is not shown in the EDX maps, as it was not relevant to the discussion. (For interpretation of the references to colour in this figure legend, the reader is referred to the web version of this article.)

than at 850 °C, the Cr evaporation data shown in the present work strongly suggest that the Ce/Co coating has self-healing capabilities also at these lower temperatures. Additionally, the initial Cr evaporation rates of the deformed Ce/Co-coated AISI 441 at those low temperatures were substantially lower than the rates for the uncoated material because most of the surface was still covered with undamaged coating. To what extent the initially higher Cr evaporation is acceptable or not is difficult to establish due to the lack of studies correlating Cr evaporation to stack degradation. At 650 °C the additional Cr evaporation is estimated to be $3 \cdot 10^{-3} \text{ mg cm}^{-2}$ based on the data presented in Fig. 1. According to an estimate by Stanislawski et al. [21] this would correspond to less than 1% cell degradation in the stack Research Centre Juelich build around 2006. This shows further studies are needed to elucidate the relationship between Cr evaporation and cell and stack degradation. A detailed discussion of the behavior of the deformed Ce/Co-coated AISI 441 at 750 and 650 °C is given below.

The Cr evaporation data for 750 °C suggests that the cracks were healed after 71 h, because the rate in the interval between 71 and 168 h already exhibited Cr evaporation rates as low as the undeformed material. This was further confirmed with STEM/EDX analysis of the lift-out, which was prepared after 71 h of exposure at 750 °C (see Fig. 5). This analysis showed that a comparatively thick $(\text{Co,Fe,Mn})_3\text{O}_4$ (300–400 nm) layer had formed on top of the cracks. In comparison to the non-cracked region, the cracked and subsequently healed regions showed high amounts of Mn in the Co oxide layer, up to 30 cationic% compared to 5 cationic% for non-cracked regions. This is in agreement with what Falk-Windisch et al. [23,27] have reported at 850 °C. They have suggested that the increase in Mn content is due to the formation of

a thin $(\text{Cr,Mn})_3\text{O}_4$ layer first as the top layer of the crack, after which lateral diffusion of Co into the crack occurs and leads to the enrichment of Co in the outer oxide layer. In the present study additional SEM/EDX analysis of the deformed Ce/Co-coated AISI 441 exposed for 500 h at 750 °C (see Fig. 4) showed that Co completely covered the entire sample surface with the cracks nearly invisible. This confirms that all the cracks had healed sufficiently well after this long exposure time.

The process of self-healing was significantly slower at 650 °C, and according to the Cr evaporation data the process seemed to be complete only after 360 h of exposure. Additionally, the decrease in the Cr evaporation rate between the first recorded value and the value at which stability was reached was much steeper at 650 °C than at 750 °C. In fact, the first recorded Cr evaporation rate for the deformed Ce/Co-coated AISI 441 was higher at 650 °C than that at 750 °C, suggesting that the cracks at the lower temperature had not sufficiently healed to decrease Cr evaporation. This was further confirmed by the difference in factor, which defined the decrease in Cr evaporation rate at both temperatures. While this factor was close to 2 at 750 °C, it was nearly 4 times higher at 650 °C. A lift-out of a specimen exposed for a short time (111 h) 650 °C was investigated using STEM/EDX (see Fig. 8). A very thin Co,Cr,Fe,Mn oxide layer had formed inside the crack, and again rather high Mn levels were measured, similar to the deformed samples exposed at 750 °C. The results suggest that at 650 °C and after 111 h of exposure self-healing of the cracks is still progressing. This matches well with the ongoing decrease of the Cr evaporation rate. The SEM/EDX data collected after 500 h of exposure back up this claim (see Fig. 6), because the cracks were still clearly visible in the EDX maps even after this time interval. This suggests that the Co layer in the cracked areas was so thin that the

electron beam penetrated it which resulted in signal generation by the underlying steel. Nevertheless, the presence of a Co rich oxide was confirmed in the linescan in Fig. 8. This correlates well with the Cr evaporation rate that dropped sharply after 111 h and reached the same level for the deformed Ce/Co-coated AISI 441 as for the undeformed material after 360 h. This validates that after 360 h enough Co had diffused into the cracks for good protection against Cr evaporation.

At 650 °C a secondary issue arose, the formation of Fe-rich nodules on the entire sample surface (see Fig. 6 and Fig. 7). These nodules resembled features that Falk-Windisch et al. [35,37] have reported on previously. In their study, these features only formed at 650 °C and when no Ce coating had been applied or when there had been no pre-oxidation step prior to coating. Those authors have explained the occurrence of these Fe-rich nodules as the metallic interdiffusion that occurs between the Co coating and the steel substrate in the initial stages of oxidation, which takes much longer at lower temperatures than at higher temperatures. Furthermore, they have shown that this interdiffusion can be avoided either by pre-oxidation before depositing a Co coating or by having a Ce coating in between the Co coating and the steel substrate. It is speculated that a similar mechanism applies in the present work. If cracks form inside the Ce layer due to the deformation process, the appearance of nodules during exposure at 650 °C would be an expected consequence, due to the lack of a diffusion barrier. This theory becomes even more plausible when the STEM/EDX maps for the deformed material are studied. Very low Ce signals were detected inside the crack at both 750 °C (see Fig. 5c) and 650 °C (see Fig. 8c). These signals were not visible in the maps at all and could only be seen in the line scans. However, Ce was clearly visible in the EDX maps of non-cracked areas. This strongly suggests that the nodule formation was probably due to the lack of Ce between the Co coating and the steel substrate. Additionally, also the results of heat-treated deformed Ce/Co coated AISI 441 validates this theory (see Fig. 6). As mentioned earlier Falk-Windisch et al. [35] showed that the formation of these Fe-rich oxide layers occurred during the first hour of oxidation at 650 °C. In the present work the heat-treated samples were first oxidized for 3 h at 850 °C, therefore the initial oxidation step at 650 °C was avoided and the formation of Fe-rich oxide nodules was mitigated (see Fig. 6b).

It should be stressed that the presence of Fe-rich oxide nodules did not impact the Cr evaporation rate negatively (see Fig. 1c and c1). This is probably due to the fact that the nodules were covered in a rather pure Co_3O_4 spinel, with 10 at.% Fe, but no Cr. Hence, these nodules are not expected to have any negative influence on Cr evaporation in the long run. Nevertheless, for technical applications the formation of Fe-rich oxide nodules might lead to other issues, for example an increase in electrical resistance or a contact loss to other fuel cell parts. However, because heat treatment seems to completely mitigate the formation of these features, these problems might never arise in real fuel cell applications. This is due to the fact that fuel cell stacks are heat-treated before the first start-up to achieve sealing of the stack. This conditioning step is typically carried out in air and at temperatures around $800\text{ °C} \pm 75\text{ °C}$ (manufacturer-dependent). Therefore, the conditioning step has a similar effect on coated and deformed interconnect than the heat treatment used in the present work. Thus, the formation of Fe-rich oxide nodules is mitigated under real conditions.

5. Conclusion

The present study has shown that the cracks formed during the deformation of Ce/Co-coated AISI 441 healed during exposure to air at low temperatures, i.e. 650, and 750 °C. The Cr evaporation data showed that the healing step was completed after 71 h of exposure at 750 °C and 360 h of exposure at 650 °C. Even though the initial Cr evaporation rates were higher for the deformed material than for the undeformed material, they were still much lower than the rates for the uncoated material and are therefore not expected to lead to cathode poisoning of the fuel cell. Microscopy data also confirmed that healing was successful because

a Co oxide layer had formed on top of all the cracked areas after 500 h of exposure. It was further shown that the increased initial Cr-evaporation rates found for deformed Ce/Co coated AISI 441 can be avoided by introducing a heat treatment step at a higher temperature prior to exposure. In real applications this heat treatment can easily be achieved during sealing of the stack. Fe-rich oxide nodules had formed on the deformed Ce/Co-coated AISI 441 during exposure at 650 °C. The reason these features had formed was probably due to a crack in the Ce layer. The presence of these nodules did not impact the Cr evaporation rates of the material and heat treatment prior to exposure suppressed the formation of these Fe-rich nodules completely.

In the present work it was shown that self-healing of a Ce/Co coating occurs also at temperatures below 850 °C. This finding means that pre-coated Ce/Co materials can also be used as interconnects in IT-SOFC applications. This would lead to a drastic reduction in manufacturing cost as large-scale, roll-to-roll manufacturing processes could be applied.

CRediT authorship contribution statement

Claudia Goebel: Conceptualization, Investigation, Formal Analysis, Writing - original draft, Writing - review & editing.

Jan-Erik Svensson: Conceptualization, Supervision, Funding acquisition.

Jan Froitzheim: Conceptualization, Writing - review & editing, Funding acquisition, Supervision, Project administration.

Vijayshankar Asokan: Investigation, Formal Analysis.

Sarah Khieu: Investigation.

Declaration of competing interest

The authors declare that they have no known competing financial interests or personal relationships that could have appeared to influence the work reported in this paper.

Acknowledgments

The authors are grateful for funding by the Swedish Energy Agency (grant 2015-009652), the Fordonsstrategisk forskning och innovation (FFI), Vinnova, Sweden program, as well as the Swedish High Temperature Corrosion Centre. Furthermore, this project has received funding from the Fuel Cells and Hydrogen 2 Joint Undertaking under Grant Agreement No 826323. This Joint Undertaking receives support from the European Union's Horizon 2020 Research and Innovation program, Hydrogen Europe and Hydrogen Europe Research. This work was performed in part at the Chalmers Material Analysis Laboratory, CMAL.

References

- [1] A.B. Stambouli, E. Traversa, *Renew. Sust. Energ. Rev.* 6 (2002) 433–455, [https://doi.org/10.1016/S1364-0321\(02\)00014-X](https://doi.org/10.1016/S1364-0321(02)00014-X).
- [2] A. Kirubakaran, S. Jain, R.K. Nema, *Renew. Sust. Energ. Rev.* 13 (2009) 2430–2440, <https://doi.org/10.1016/j.rser.2009.04.004>.
- [3] J.W. Fergus, *Mater. Sci. Eng. A* 397 (2005) 271–283, <https://doi.org/10.1016/j.msea.2005.02.047>.
- [4] D.J.L. Brett, A. Atkinson, N.P. Brandon, S.J. Skinner, *Chem. Soc. Rev.* 37 (2008) 1568–1578, <https://doi.org/10.1039/b612060c>.
- [5] L. Niewolak, F. Tietz, W.J. Quadackers, *Interconnects*, in: *High-Temperature Solid Oxide Fuel Cells for the 21st Century: Fundamentals, Design and Applications*, 2015.
- [6] W.J. Quadackers, J. Piron-Abellan, V. Shemet, L. Singheiser, *Mater. High Temp.* 20 (2003) 115–127, <https://doi.org/10.1179/mht.2003.015>.
- [7] Ernest Lawrence Berkeley National Laboratory Contract No. DE-AC02-05CH11231, A Total Cost of Ownership Model for Solid Oxide Fuel Cells in Combined Heat and Power and Power-Only Applications, 2015.
- [8] Battelle Memorial Institute, *Manufacturing Cost Analysis of 100 and 250 Kw Fuel Cell Systems for Primary Power and Combined Heat and Power Applications*, 2016.
- [9] H. Falk-Windisch, J.-E. Svensson, J. Froitzheim, *J. Power Sources* 287 (2015) 25–35, <https://doi.org/10.1016/j.jpowsour.2015.04.040>.
- [10] R. Sachitanand, M. Sattari, J.-E. Svensson, J. Froitzheim, *Int. J. Hydrog. Energy* 38 (2013) 15328–15334, <https://doi.org/10.1016/j.ijhydene.2013.09.044>.

- [11] H.U. Anderson, F. Tietz, Interconnects, in: S.C. Singhal, K. Kendall (Eds.), *High Temperature Solid Oxide Fuel Cells - Fundamentals, Design and Applications*, Elsevier, Oxford, 2003.
- [12] P.Y. Hou, J. Stringer, *Mater. Sci. Eng. A* 202 (1995) 1–10, [https://doi.org/10.1016/0921-5093\(95\)09798-8](https://doi.org/10.1016/0921-5093(95)09798-8).
- [13] K. Huang, P.Y. Hou, J.B. Goodenough, *Mater. Res. Bull.* 36 (2001) 81–95, [https://doi.org/10.1016/S0025-5408\(01\)00506-2](https://doi.org/10.1016/S0025-5408(01)00506-2).
- [14] J.G. Grolig, J. Froitzheim, J.-E. Svensson, *J. Power Sources* 248 (2014) 1007–1013, <https://doi.org/10.1016/j.jpowsour.2013.08.089>.
- [15] V. Sauchuk, S. Megel, E. Girdauskaite, N. Trofimenko, M. Kusnezoff, A. Michaelis, *Russ. J. Electrochem.* 47 (2011) 522, <https://doi.org/10.1134/S1023193511050107>.
- [16] Z. Yang, M. Guo, N. Wang, C. Ma, J. Wang, M. Han, *Int. J. Hydrog. Energy* 42 (2017) 24948–24959, <https://doi.org/10.1016/j.ijhydene.2017.08.057>.
- [17] H. Kurokawa, C.P. Jacobson, L.C. DeJonghe, S.J. Visco, *Solid State Ionics* 178 (2007) 287–296, <https://doi.org/10.1016/j.ssi.2006.12.010>.
- [18] R. Trebbels, T. Markus, L. Singheiser, *J. Electrochem. Soc.* 157 (2010) B490–B495, <https://doi.org/10.1149/1.3298434>.
- [19] J. Froitzheim, J.-E. Svensson, *ECS Trans.* 35 (2011) 2503–2508, <https://doi.org/10.1149/1.3570248>.
- [20] A. Petric, H. Ling, *J. Am. Ceram. Soc.* 90 (2007) 1515–1520, <https://doi.org/10.1111/j.1551-2916.2007.01522.x>.
- [21] M. Stanislawski, J. Froitzheim, L. Niewolak, W.J. Quadackers, K. Hilpert, T. Markus, L. Singheiser, *J. Power Sources* 164 (2007) 578–589, <https://doi.org/10.1016/j.jpowsour.2006.08.013>.
- [22] J. Froitzheim, S. Canovic, M. Nikumaa, R. Sachitanand, L.G. Johansson, J. E. Svensson, *J. Power Sources* 220 (2012) 217–227, <https://doi.org/10.1016/j.jpowsour.2012.06.092>.
- [23] H. Falk-Windisch, M. Sattari, J.-E. Svensson, J. Froitzheim, *J. Power Sources* 297 (2015) 217–223, <https://doi.org/10.1016/j.jpowsour.2015.07.085>.
- [24] F.Q. Li, J.Y. Du, L.H. Zhang, J. Li, G.P. Li, G.H. Zhu, M.G. Ouyang, J.S. Chai, H. Li, *Int. J. Hydrog. Energy* 42 (2017) 29966–29970, <https://doi.org/10.1016/j.ijhydene.2017.06.226>.
- [25] Z. Yang, G. Xia, S.P. Simner, J.W. Stevenson, *J. Electrochem. Soc.* 152 (2005) A1896, <https://doi.org/10.1149/1.1990462>.
- [26] L.V. Gambino, N.J. Magdefrau, M. Aindow, *Mater. High Temp.* 32 (2015) 142–147, <https://doi.org/10.1179/0960340914z.00000000090>.
- [27] H. Falk-Windisch, I. Mertzidis, J.-E. Svensson, J. Froitzheim, *ECS Trans.* 68 (2015) 1617–1623, <https://doi.org/10.1149/06801.1617ecst>.
- [28] N.B. Pilling, R.E. Bedworth, *J. Inst. Met.* 29 (1923) 529–582, <https://doi.org/10.1098/rspa.1926.0062>.
- [29] Z. Grzesik, A. Kaczmarek, S. Mrowec, *Solid State Phenom.* 227 (2015) 421–424, <https://doi.org/10.4028/www.scientific.net/SSP.227.421>.
- [30] L. Niewolak, E. Wessel, L. Singheiser, W.J. Quadackers, *J. Power Sources* 195 (2010) 7600–7608, <https://doi.org/10.1016/j.jpowsour.2010.06.007>.
- [31] M. Torkar, F. Tehovnik, B. Podgornik, *Eng. Fail. Anal.* 40 (2014) 1–7.
- [32] J. Froitzheim, H. Ravash, E. Larsson, L.G. Johansson, J.-E. Svensson, *J. Electrochem. Soc.* 157 (2010) B1295–B1300, <https://doi.org/10.1149/1.3462987>.
- [33] S. Canovic, J. Froitzheim, R. Sachitanand, M. Nikumaa, M. Halvarsson, L. G. Johansson, J.-E. Svensson, *Surf. Coat. Technol.* 215 (2013) 62–74, <https://doi.org/10.1016/j.surfcoat.2012.08.096>.
- [34] C. Goebel, A.G. Fefekos, J.-E. Svensson, J. Froitzheim, *J. Power Sources* 383 (2018) 110–114, <https://doi.org/10.1016/j.jpowsour.2018.02.060>.
- [35] H. Falk-Windisch, J. Claquesin, J.-E. Svensson, J. Froitzheim, *Oxid. Met.* 89 (2018) 233–250, <https://doi.org/10.1007/s11085-017-9782-9>.
- [36] E. McCafferty, *Introduction to Corrosion Science*, 1 ed., Springer, New York, 2010.
- [37] H. Falk-Windisch, J. Claquesin, M. Sattari, J.-E. Svensson, J. Froitzheim, *J. Power Sources* 343 (2017) 1–10, <https://doi.org/10.1016/j.jpowsour.2017.01.045>.